EUROPEAN ORGANIZATION FOR NUCLEAR RESEARCH (CERN)

Search for the rare decays $W^+ \to D_s^+ \gamma$ and $Z \to D^0 \gamma$ at LHCb

LHCb collaboration

Abstract

A search for the rare decays $W^+ \to D_s^+ \gamma$ and $Z \to D^0 \gamma$ is performed using proton-proton collision data collected by the LHCb experiment at a centre-of-mass energy of $13 \, \text{TeV}$, corresponding to an integrated luminosity of $2.0 \, \text{fb}^{-1}$. No significant signal is observed for either decay mode and upper limits on their branching fractions are set using $W^+ \to \mu^+ \nu$ and $Z \to \mu^+ \mu^-$ decays as normalization channels. The upper limits are 6.5×10^{-4} and 2.1×10^{-3} at 95% confidence level for the $W^+ \to D_s^+ \gamma$ and $Z \to D^0 \gamma$ decay modes, respectively. This is the first reported search for the $Z \to D^0 \gamma$ decay, while the upper limit on the $W^+ \to D_s^+ \gamma$ branching fraction improves upon the previous best limit.

Submitted to Chin. Phys. C

1 Introduction

The large production cross-sections of W and Z bosons at hadron colliders offer unique opportunities to search for their rare decays, which can be used to test the Standard Model (SM) and probe for physics beyond the SM. Particularly interesting are the radiative decays of the W and Z bosons, predictions of their branching fractions using the quantum chromodynamics (QCD) factorization [1–6] range from 10^{-6} to 10^{-12}. Unlike in B-meson decays, where large power corrections to the decay rates lead to sizable theoretical uncertainties, power corrections in W and Z boson decays are under good control due to the large energy released to the final state hadrons. Thus, the study of hadronic-radiative W and Z bosons decays can provide stringent tests of the QCD factorization formalism [5]. After almost forty years from the discoveries of the W and Z bosons, no hadronic-radiative decay of these bosons has been observed, despite searches performed by the ATLAS [7–10], CMS [11, 12], and CDF [13] collaborations. The current best limit is 9×10^{-7} for the branching fraction of the $Z \to \phi\gamma$ decay [8].

This paper presents searches for the radiative decays $W^+ \to D_s^+\gamma$ and $Z \to D^0\gamma$, followed by $D_s^+ \to K^+K^-\pi^+$ and $D^0 \to K^-\pi^+$, at the LHCb experiment, taking advantage of its excellent hadron identification capabilities.[1]

The radiative decay $W^+ \to D_s^+\gamma$ can proceed via tree-level diagrams as shown in Fig. 1 and its branching fraction is predicted to be $(3.7 \pm 1.5) \times 10^{-8}$ in the SM [5]. A previous search for this decay by the CDF collaboration found no significant signal and determined the limit $\mathcal{B}(W^+ \to D_s^+\gamma) < 1.3 \times 10^{-3}$ at 95% confidence level [13].
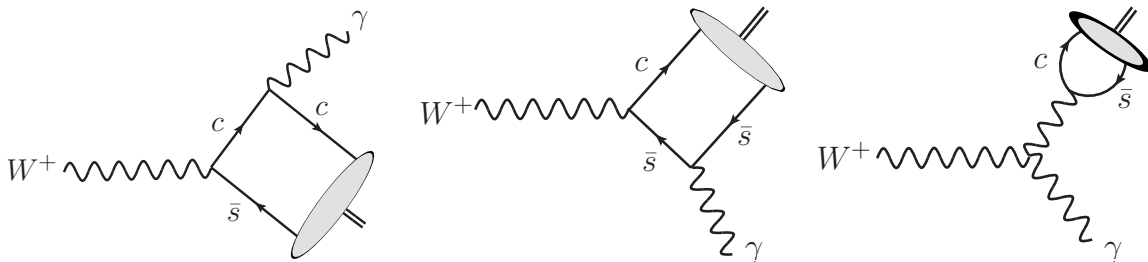

Figure 1: Tree-level Feynman diagrams for the decay $W^+ \to D_s^+\gamma$.

The radiative decay $Z \to D^0\gamma$ is a flavour-changing-neutral-current (FCNC) process, forbidden at the tree level, and can only proceed via higher-order loop processes in the SM, as shown in Fig. 2. The FCNC couplings of Z boson are heavily constrained by the existing precision measurements from flavour physics, resulting in a negligible branching fraction ($\mathcal{O} \sim 10^{-15}$) of $Z \to D^0\gamma$ mode. However, a search for this decay can provide a model-independent way to probe the FCNC couplings of the Z boson [14]. To date, there is no experimental study of this process.

The search uses data from proton-proton collisions at $13\,\mathrm{TeV}$ collected by the LHCb experiment, corresponding to a luminosity of $2.0\,\mathrm{fb}^{-1}$. These data were collected in 2018 when the trigger selection dedicated to these decays was implemented. Both relative and absolute branching fractions of the decays $W^+ \to D_s^+\gamma$ and $Z \to D^0\gamma$ are determined, using $W^+ \to \mu^+\nu$ and $Z \to \mu^+\mu^-$ decays as normalization channels,

---

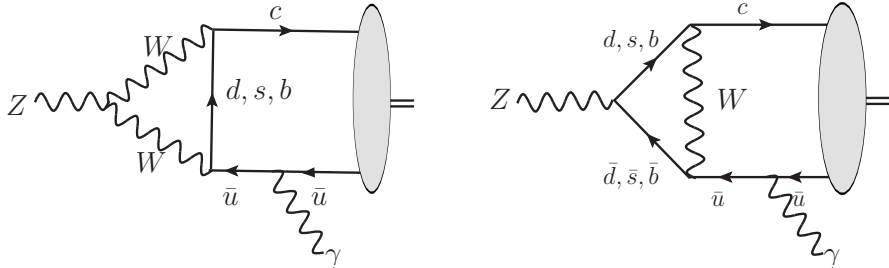[1]The inclusion of charge-conjugate processes is implied throughout.

Figure 2: Feynman diagrams contributing to the $Z \to D^0 \gamma$ decay in the SM.

respectively. In this article, the fiducial criteria require that the particle lie within the LHCb acceptance, $10 < \theta < 400$ mrad for the charged particles, and $25 < \theta_x < 300$ mrad and $25 < \theta_y < 250$ mrad for the neutral particles, where θ is the polar angle with respect to the beam direction and $\theta_{x(y)}$ is the projection of the polar angle on the xz (yz) plane.

2 Detector and simulation

The LHCb detector [15, 16] is a single-arm forward spectrometer covering the pseudorapidity range $2 < \eta < 5$, designed for the study of particles containing b or c quarks. The detector includes a high-precision tracking system consisting of a silicon-strip vertex detector surrounding the pp interaction region [17], a large-area silicon-strip detector located upstream of a dipole magnet with a bending power of about 4 Tm, and three stations of silicon-strip detectors and straw drift tubes [18, 19] placed downstream of the magnet. The tracking system provides a measurement of the momentum, p, of charged particles with a relative uncertainty that varies from 0.5% at low momentum to 1.0% at 200 GeV/c. The minimum distance of a track to a primary pp collision vertex (PV), the impact parameter (IP), is measured with a resolution of $(15 + 29/p_T)$ μm, where p_T is the component of the momentum transverse to the beam, in GeV/c. Different types of charged hadrons are distinguished using information from two ring-imaging Cherenkov detectors [20]. Photons, electrons and hadrons are identified by a calorimeter system consisting of scintillating-pad and preshower detectors, an electromagnetic and a hadronic calorimeter [16, 21]. Charged and neutral clusters in the electromagnetic calorimeter are discerned by extrapolating the tracks reconstructed by the tracking system to the calorimeter plane. Photon and neutral pions are distinguished by cluster shape and energy distribution. The read-out electronics of the electromagnetic calorimeter is optimised for the typical energy deposits that occur in LHCb, *i.e.* heavy flavour physics, which results in a maximum detectable transverse energy of 10 GeV. A photon with very high energy is expected to have at least one saturated calorimeter cell. Photons and neutral pions are distinguished by cluster shape, energy and mass distributions. Muons are identified by a system composed of alternating layers of iron and multiwire proportional chambers [22].

The online event selection is performed by a trigger, which consists of a hardware stage followed by a two-level software stage. In between the two software stages, an alignment and calibration of the detector is performed in near real-time and their results are used in the trigger [23]. The same alignment and calibration information is propagated to the offline reconstruction, ensuring a consistent and high quality reconstruction and event

selection between the trigger and offline software. The identical performance of the online and offline reconstruction offers the opportunity to perform physics analyses directly using candidates reconstructed in the trigger [24, 25], which the present analysis exploits to reduce the event size by one order of magnitude.

Simulation is required to model the effects of the detector acceptance and the imposed selection requirements. In the simulation, pp collisions are generated using PYTHIA [26] with a specific LHCb configuration [27]. Decays of unstable particles are described by EVTGEN [28], in which final-state radiation is generated using PHOTOS [29]. The interaction of the generated particles with the detector, and its response, are implemented using the GEANT4 toolkit [30] as described in Ref. [31]. In the signal simulation, the decay probability of $D_s^+ \to K^+ K^- \pi^+$ is taken to be uniform across the available phase space. However, there are sizable resonance contributions in the D_s^+ decay, which are accounted for by assigning weights to the simulated candidates.

3 Reconstruction and selection

The $W^+ \to D_s^+ (\to K^+ K^- \pi^+) \gamma$ and $Z \to D^0 (\to K^- \pi^+) \gamma$ candidates must be matched to a positive decision in the hardware trigger. which selects events by exploiting the particular signature of a photon with a high-energy cluster in the electromagnetic calorimeter and hadrons with high-transverse-energy deposits, E_T, in the calorimeters.

In the first software trigger stage, the charged final-state particles are required to be inconsistent with originating from a PV, and are further required to pass a boosted decision tree (BDT) multivariate selector [32], where the input variables rely on transverse momentum, vertex fit quality, and flight distance information for D_s^+ and D^0 candidates. In the second software trigger stage, $D_s^+ \to K^+ K^- \pi^+$ candidates are reconstructed from three tracks each with $p_T > 0.25\,\text{GeV}/c$. To further suppress background, additional requirements are applied to the combination of tracks, by requiring at least one of the three tracks to have p_T greater than $1.0\,\text{GeV}/c$, at least two of them to have p_T greater than $0.4\,\text{GeV}/c$, and the scalar p_T sum of the three tracks to be greater than $3\,\text{GeV}/c$. The D_s^+ candidate is required to have a reconstructed invariant mass in the range $[1.879, 2.059]\,\text{GeV}/c^2$, and $p_T > 15\,\text{GeV}/c$. The D_s^+ candidate is further required to have a good vertex fit quality, and the D_s^+ vertex is required to be displaced from every PV by a distance corresponding to a D_s^+ decay time larger than $0.2\,\text{ps}$. An additional neutral particle, which must be identified as a photon and have E_T greater than $10\,\text{GeV}$, is then combined with the D_s^+ candidate to form a $W^+ \to D_s^+ (\to K^+ K^- \pi^+) \gamma$ candidate. The W candidate must have invariant mass between 30 and $130\,\text{GeV}/c^2$. Similarly, $D^0 \to K^- \pi^+$ candidates are reconstructed from two tracks that pass track quality requirements, with $p_T > 0.5\,\text{GeV}/c$ and $p > 5\,\text{GeV}/c$. The D^0 candidate is required to have reconstructed mass in the range $[1.715, 2.015]\,\text{GeV}/c^2$, and p_T greater than $15\,\text{GeV}/c$. The D^0 candidate must have a good vertex fit quality and must be displaced from every PV. Each $Z \to D^0 (\to K^- \pi^+) \gamma$ candidate is reconstructed from a D^0 candidate plus a photon with $E_T > 10\,\text{GeV}$. The Z boson candidates are required to have the invariant mass between 30 and $130\,\text{GeV}/c^2$.

In the offline selection, the photon candidates are required to satisfy $E_T > 15\,\text{GeV}$. Background due to photons from π^0 decays is rejected by a dedicated algorithm [33]. The final-state particles associated with the $D_s^+ \to K^+ K^- \pi^+$ candidates are further required to have p_T greater than $0.5\,\text{GeV}/c$ and be located within the LHCb fiducial region. Two

opposite-charged tracks are required to be identified as kaon tracks. The D_s^+ mass region is restricted to the range [1.92, 2.02] GeV/c^2, while the D_s^+ p_T is required to be greater than 20 GeV/c. A similar offline selection is applied to the $D^0 \rightarrow K^-\pi^+$ candidates, with the D^0 mass window requirement fixed to [1.82, 1.92] GeV/c^2. Contamination from decays of other particles is suppressed by dedicated mass veto requirements. The decay $D^+ \rightarrow K^-\pi^+\pi^+$, with a charged pion misidentified as a kaon, could contribute to the $D_s^+ \rightarrow K^+K^-\pi^+$ decay. Similarly the decay $D^{*+} \rightarrow D^0(\rightarrow K^+K^-)\pi^+$ with the same final-state particles but different peak positions, could also contribute to the selected D_s^+ candidates. A mass veto requirement $|M(K^-\pi^+\pi^+) - 1.870| > 0.02$ GeV/c^2 is employed to reject the D^+ background. The background contribution from the D^{*+} process is removed with the condition $M(K^+K^-) < 1.85$ GeV/c^2. The background contribution from $\Lambda_c^+ \rightarrow pK^-\pi^+$ decay is studied and found to be well described as part of the combinatorial background.

The event selection of the normalization channels is similar to that used in previous LHCb publications [34, 35]. The online event selection is performed with the single muon triggers. At the hardware trigger stage, events are required to include a muon with high p_T. The muon candidate must satisfy $p_T > 6$ GeV/c, $p > 8$ GeV/c, with a good track fit quality in the first software trigger stage. In the second software trigger stage, the muon candidate is further required to satisfy $p_T > 12.5$ GeV/c. For a $W^+ \rightarrow \mu^+\nu$ candidate, the muon is required to pass all three single-muon trigger decision stages, and for a $Z \rightarrow \mu^+\mu^-$ candidate, at least one of the muons must pass all three decision stages.

The offline $W^+ \rightarrow \mu^+\nu$ candidate selection starts by requiring events to have a well-reconstructed muon candidate with p_T between 20 and 70 GeV/c. The relative uncertainty in the momentum measurement for the muon is required to be less than 10%. Different background contributions have been considered and specific selection conditions have been devised in order to suppress the various contributions. Since a muon from a W^+ boson decay is typically isolated from other particles, an isolation requirement is applied on the muon to suppress background contributions, where one muon is originating from a QCD process. To reduce the contamination from $Z \rightarrow \mu^+\mu^-$ decays, events are required to have no additional muon candidate with p_T above 2 GeV/c. Background contamination from $Z \rightarrow \tau^+\tau^-$ and heavy-flavour events is suppressed by requiring the IP of the muon candidate to be smaller than 40 μm. Muons from W boson decay, which tend to be highly isolated, are associated with low energy deposits in the electromagnetic and hadronic calorimeters. Therefore, the amount of energy that is deposited in the calorimeters relative to the momentum of the track is required to be smaller than 4%, which reduces the background from energetic pions and kaons punching through the calorimeters to the muon stations. In total, 4.4 million $W^+ \rightarrow \mu^+\nu$ candidates are selected.

For the $Z \rightarrow \mu^+\mu^-$ offline selection, the candidates are required to have a pair of well-reconstructed tracks of opposite charge identified as muons. Muon tracks must have a p_T greater than 20 GeV/c and $2.0 < \eta < 4.5$. The invariant mass of the two muons must be in the range of 60 to 120 GeV/c^2. The relative uncertainty in the momentum measurement for each muon is required to be less than 10%. In total, 320 000 $Z \rightarrow \mu^+\mu^-$ candidates are selected.

4 Yield determination

To determine the yields of W^+ and Z candidates, the pseudomass is used. Similarly to the one used in Ref. [36], it is defined as

$$m(M\gamma) = \sqrt{2p^M p_T^M \frac{p^\gamma}{p_T^\gamma}(1 - \cos\theta)}, \qquad (1)$$

where p^M and p_T^M are the momenta and transverse momenta of the meson, p^γ and p_T^γ are the momenta and transverse momenta of the photon, and θ is the opening angle between the meson and the photon. The pseudomass is an approximation of the invariant mass in which the photon energy, which is poorly measured for transverse energies above the saturation value, is cancelled, resulting in more than 5% improvement on the expected upper limit. The selected $W^+ \to D_s^+ \gamma$ candidates with pseudomass between 35 and 120 GeV/c^2, and the selected $Z \to D^0 \gamma$ candidates with pseudomass between 50 and 125 GeV/c^2 are used in the yield determination. An extended maximum-likelihood method is adopted, with the finite template statistics accounted for, according to Ref. [37]. Upper limits on the signal yields are determined with the CL_S method [38, 39], using the candidate pseudomass and p_T distributions, and their correlations. The upper limits are calculated at 95% confidence level (C.L.), with the asymptotic CL_S method in the RooStats framework [40, 41] taking into account systematic uncertainties.

The signal shapes are determined from simulation, after event selection. The background shape is estimated using a background-dominated sample, following a data-driven method used previously by the ATLAS collaboration [42, 43]. The background-dominated data sample is selected using candidates in the meson invariant mass sideband, with the requirement on the meson p_T changed from 20 GeV/c to 15 GeV/c. Since the D^0 lower mass sideband region contains other background contributions, the upper sideband region is selected $[1.91, 2.00]$ GeV/c^2 for the $Z \to D^0 \gamma$ background study. For D_s^+ candidates, both lower $[1.90, 1.94]$ GeV/c^2 and upper $[2.00, 2.05]$ GeV/c^2 sideband regions are used. Probability density functions (PDFs) are used to model the distributions of the selected background events, and correlations between different variables are taken into account using Gaussian kernel density estimation (KDE) [44]. Pseudodata candidates are generated, from which the background shape in the discriminating variable is derived. The ensemble of pseudodata candidates is produced by randomly sampling distributions of the relevant kinematic variables. These candidates are described by meson and photon four-momentum vectors:

- The meson four-momentum vector is constructed from its pseudorapidity (η_M), azimuthal angle (ϕ_M), mass (m_M), and transverse momentum (p_T^M).

- For the photon four-momentum vector, the p_T^γ of the selected photon candidate is used, while the photon pseudorapidity, η_γ, and azimuthal angle, ϕ_γ, are determined from the sampled $\Delta\eta(M, \gamma)$ and $\Delta\phi(M, \gamma)$ values, where $\Delta\eta(M, \gamma)$ and $\Delta\phi(M, \gamma)$ are the differences in η and ϕ between the meson and the photon.

The correlations among these kinematic variables in background events are retained in the generation of the pseudodata through the following sampling scheme:

- The η_M, ϕ_M, m_M, and p_T^M values are drawn randomly and independently according to the corresponding PDFs. In the background-dominated data samples, the

correlations between these variables are found to be negligible, therefore the variables are assumed to be uncorrelated.

- The distributions of p_T^γ, $\Delta\phi(M,\gamma)$ and $\Delta\eta(M,\gamma)$ are parameterised in bins of p_T^M, and values are drawn from the distributions of the bin corresponding to the previously generated p_T^M value.

Pseudodata candidates that pass the standard selection are used to construct two-dimensional template distributions of pseudomass and p_T.

The distributions of pseudomass and p_T for the signal candidates, overlaid with the signal and background models, are shown in Fig. 3. With no visible signal contribution, upper limits on the relative and absolute branching fractions are calculated.
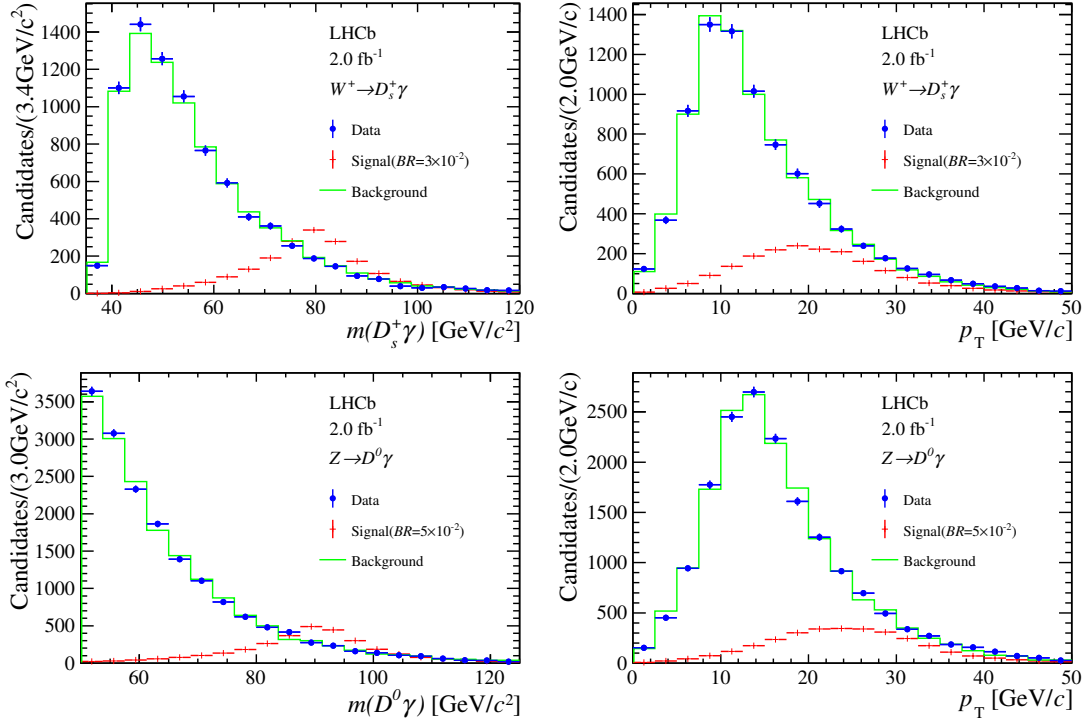

Figure 3: Distributions of (left) pseudomass and (right) p_T for (upper) $W^+ \to D_s^+\gamma$ and (lower) $Z \to D^0\gamma$ candidates. The blue points represent the selected data candidates, the red points represent simulated signal events, normalized to the branching fraction of $W^+ \to D_s^+\gamma$ ($Z \to D^0\gamma$) set to 3×10^{-2} (5×10^{-2}), and the green lines represent the background shape.

5 Ratio of branching fractions

The ratio $\mathcal{R}(W)$ of the $W^+ \to D_s^+\gamma$ branching fraction relative to that of the $W^+ \to \mu^+\nu$ decay is defined as

$$
\begin{aligned}
\mathcal{R}(W) &\equiv \frac{\mathcal{B}(W^+ \to D_s^+\gamma)}{\mathcal{B}(W^+ \to \mu^+\nu)} \\
&= \frac{N_s \times \varepsilon_n \times \mathcal{A}_n}{N_n \times \varepsilon_s \times \mathcal{A}_s} \times \frac{1}{\mathcal{B}(D_s^+ \to K^+K^-\pi^+)},
\end{aligned}
\tag{2}
$$

where $\mathcal{B}(W^+ \to D_s^+ \gamma)$ is the branching fraction of $W^+ \to D_s^+ \gamma$ decay, $\mathcal{B}(W^+ \to \mu^+ \nu)$ is the branching fraction of $W^+ \to \mu^+ \nu$ decay, and $\mathcal{B}(D_s^+ \to K^+ K^- \pi^+)$ is the branching fraction of $D_s^+ \to K^+ K^- \pi^+$ process; N_s (N_n) is the total signal (normalization) yield after background subtraction; $\mathcal{A}_s$ ($\mathcal{A}_n$) is the probability for the true W boson decay charged products momenta to lie within the LHCb acceptance, ε_s (ε_n) is the total trigger, reconstruction and selection efficiency of the signal (normalization) channel.

The equivalent ratio of branching fractions, $\mathcal{R}(Z)$, and absolute branching fraction of the $Z \to D^0 \gamma$ decay are studied using the $Z \to \mu^+ \mu^-$ decay as a normalization channel. With the requirement that the final-state particle must be in the LHCb detector fiducial region, the definition can be written as

$$
\begin{aligned}
\mathcal{R}(Z) \quad &\equiv \quad \frac{\mathcal{B}(Z \to D^0 \gamma)}{\mathcal{B}(Z \to \mu^+ \mu^-)} \\
&= \quad \frac{N_s \times \varepsilon_n \times \mathcal{A}_n}{N_n \times \varepsilon_s \times \mathcal{A}_s} \times \frac{1}{\mathcal{B}(D^0 \to K^- \pi^+)},
\end{aligned}
\tag{3}
$$

where $\mathcal{B}(Z \to D^0 \gamma)$ is the branching fraction of $Z \to D^0 \gamma$ decay, $\mathcal{B}(Z \to \mu^+ \mu^-)$ is the branching fraction of $Z \to \mu^+ \mu^-$ decay, and $\mathcal{B}(D^0 \to K^- \pi^+)$ is the branching fraction of $D^0 \to K^- \pi^+$ process.

As the number of final-state particles is different between signal and normalization channels, the acceptance correction is determined and applied to the $\mathcal{R}$ calculation. The $\mathcal{A}_s$ and $\mathcal{A}_n$ factors are evaluated using event generators. In the acceptance study, the uncertainty from parton distribution functions is taken as a systematic uncertainty. The efficiencies ε_s and ε_n are determined from control and simulated samples. For signal, the event selection efficiencies are determined from simulation, where the track detection and particle identification efficiencies are calibrated with the data [45–47]. The photon identification efficiency is calibrated using a $B^0 \to K^{*0} \gamma$ [48] control sample, where only events with a photon of $E_T > 10 \, \text{GeV}$ are used. The muon efficiencies are estimated using $Z \to \mu^+ \mu^-$ data candidates with the tag-and-probe method [35].

6 Systematic uncertainties

The systematic uncertainties in the $\mathcal{R}(W)$ and $\mathcal{R}(Z)$ measurements are summarised in Table 1. The uncertainties in the $D_s^+ \to K^+ K^- \pi^+$ and $D^0 \to K^- \pi^+$ branching fractions are 1.86% and 0.76%, respectively [49]. The uncertainties of the normalization modes are expected to be uncorrelated with the uncertainties of the signal modes. Systematic uncertainties from normalization channels are studied separately for the $W^+ \to \mu^+ \nu$ and $Z \to \mu^+ \mu^-$ channels. Uncertainties from background estimation, efficiency calculations, signal determination and limited simulation sample size are taken into account, leading to relative uncertainties of 0.96% for $Z \to \mu^+ \mu^-$ and 3.08% for $W^+ \to \mu^+ \nu$ decays in the $\mathcal{R}(W)$ and $\mathcal{R}(Z)$ measurements. The $W^+ \to D_s^+ \gamma$ simulation is corrected using the measured Dalitz-plot distribution. To determine the uncertainty from the meson decay modelling, the binning width of the reference Dalitz-plot distribution is varied by a factor of 0.75.

An uncertainty is assigned due to the limited size of the simulation samples used to determine the event selection efficiency. The PID efficiency is calibrated using a control data sample [21], and a systematic uncertainty arises due to the limited sample size.

The uncertainty is estimated by enlarging or decreasing the binning of p, η, and event multiplicity of the control sample by a factor of two. Similarly, the systematic uncertainty associated with the photon identification efficiency calibration is evaluated by varying the binning of the $B^0 \to K^{*0}\gamma$ control sample. The modelling of saturated calorimeter cells in the simulation is calibrated using $B^0 \to K^{*0}\gamma$ data events, and the systematic uncertainties from the size of the control sample and the binning schemes are studied. The combined uncertainty is determined to be 3.0% (3.1%) for $Z \to D^0\gamma$ ($W^+ \to D_s^+\gamma$). The uncertainty on the acceptance correction takes into account the size of the simulation samples, and uncertainties in the parton distribution function, combined in quadrature.

To estimate the systematic uncertainty from the background modelling, two sources are studied. The meson mass sideband regions are shifted to higher and lower masses by $0.03\,\mathrm{GeV}/c^2$, and the deviations are assigned as uncertainty. An additional uncertainty is assigned by changing the binning of the meson p_T (by a factor of up to 50%) in the non-parametric data-driven approach, using finer and coarser binnings. The uncertainty from background modelling is determined to be 0.08% (0.36%) for the $Z \to D^0\gamma$ ($W^+ \to D_s^+\gamma$) search. The PV association algorithm was updated during the data-taking period, which causes a mismatch between LHCb data and simulation, and introduces systematic effects in the efficiency estimation. A correction is studied and applied to the simulation, and an uncertainty is assigned for this correction. An additional correction is applied to the simulation to account for imperfect modelling of the resolution of the meson invariant mass, by applying a 0.5% (0.6%) smearing correction to the D_s^+ (D^0) simulation. A systematic uncertainty is evaluated by varying the resolution correction within its statistical uncertainty.

Table 1: Relative systematic uncertainties (in %) in the $\mathcal{R}$ measurements for the $Z \to D^0\gamma$ and $W^+ \to D_s^+\gamma$ decay modes. The total systematic uncertainty is obtained from the sum in quadrature of all contributions.

Source	$Z \to D^0\gamma$ (%)	$W^+ \to D_s^+\gamma$ (%)
Meson BF	0.76	1.86
Normalization	0.96	3.08
Dalitz	-	0.24
MC sample size	0.11	0.09
PID	0.09	0.17
Photon ID	2.32	0.95
Calorimeter saturation	3.00	3.10
Background	0.36	0.08
Acceptance	0.18	0.21
PV association	0.57	0.29
Resolution	0.20	0.09
Total	4.04	4.86

7   Results

No significant peaking structure is found in the inspected pseudomass ranges. The CL_S method [38, 39] is used to calculate upper limits on the branching fractions of the $W^+ \to D_s^+ \gamma$ and $Z \to D^0 \gamma$ decays. In the calculation, we use the pseudomass and p_{T} distribution of W^+/Z boson candidates as observables, the signal shape is taken from the simulation after event selection, and the background distribution is estimated using a data-driven method. The upper limit on the ratios of branching fractions are determined to be

$$\begin{aligned} \mathcal{R}(Z) &< 6.4 \times 10^{-2} \text{ at } 95\% \text{ C.L.}, \\ \mathcal{R}(W) &< 6.1 \times 10^{-3} \text{ at } 95\% \text{ C.L.} \end{aligned}$$

The calculated and expected CL_S exclusions are shown as a function of the branching fraction for $W^+ \to D_s^+ \gamma$ and $Z \to D^0 \gamma$ decays in Fig. 4. The upper limits on the $W^+ \to D_s^+ \gamma$ and $Z \to D^0 \gamma$ rare decay branching fractions are determined to be

$$\begin{aligned} \mathcal{B}(Z \to D^0 \gamma) &< 2.1 \times 10^{-3} \text{ at } 95\% \text{ C.L.}, \\ \mathcal{B}(W^+ \to D_s^+ \gamma) &< 6.5 \times 10^{-4} \text{ at } 95\% \text{ C.L.}, \end{aligned}$$

using the known values [49] of the $Z \to \mu^+ \mu^-$ and $W^+ \to \mu^+ \nu$ branching ratios. The expected upper limit on the branching fraction is calculated to be 1.2×10^{-3} (1.9×10^{-3}) for the $W^+ \to D_s^+ \gamma$ ($Z \to D^0 \gamma$) decay.

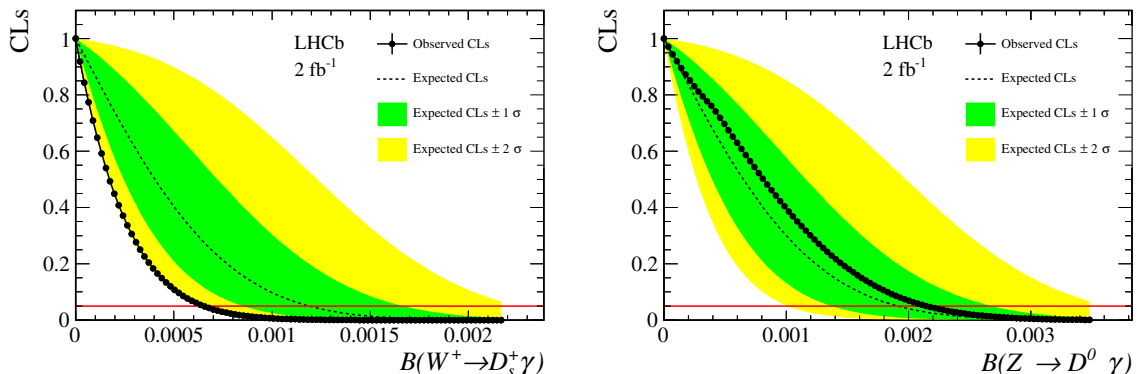
Figure 4: Upper limits on branching fractions of the (left) $W^+ \to D_s^+ \gamma$ and (right) $Z \to D^0 \gamma$ decays.

8   Conclusion

Searches for the decays $W^+ \to D_s^+ \gamma$ and $Z \to D^0 \gamma$ are performed using pp collision data at $\sqrt{s} = 13 \,\mathrm{TeV}$ collected by the LHCb experiment in 2018, corresponding to an integrated luminosity of $2.0 \,\mathrm{fb}^{-1}$. No significant signal is observed above background. For the $W^+ \to D_s^+ \gamma$ decay, the upper limit is determined to be 6.5×10^{-4} at 95% C.L., which is the best limit to date. The first search for the decay $Z \to D^0 \gamma$ is performed, and the upper limit is determined to be 2.1×10^{-3} at 95% C.L. These limits are well above the

range of their SM predictions. The next upgrade of the LHCb detector [50] will allow operation at a much higher instantaneous luminosity ($2 \times 10^{34}\ cm^{-2}s^{-1}$), while keeping good performance in reconstructing and identifying hadrons of different species. This upgrade will be well-suited for further study of these very rare decays of the W and Z bosons.

References

[1] B. Guberina, J. H. Kuhn, R. D. Peccei, and R. Ruckl, *Rare decays of the Z^0*, Nucl. Phys. **B174** (1980) 317.

[2] N. N. Achasov, *The $Z \to c\bar{c} \to \gamma\gamma^*$, $Z \to b\bar{b} \to \gamma\gamma^*$ triangle diagrams and the $Z \to \gamma\psi$, $Z \to \gamma\Upsilon$ decays*, Theor. Math. Phys. **170** (2012) 39, [Teor. Mat. Fiz.170,49(2012)].

[3] T.-C. Huang and F. Petriello, *Rare exclusive decays of the Z-boson revisited*, Phys. Rev. **D92** (2015) 014007, arXiv:1411.5924.

[4] L. Arnellos, W. J. Marciano, and Z. Parsa, *Radiative decays $W^\pm \to \rho^\pm\gamma$ and $Z^0 \to \rho^0\gamma$*, Nucl. Phys. **B196** (1982) 378.

[5] Y. Grossman, M. König, and M. Neubert, *Exclusive radiative decays of W and Z bosons in QCD Factorization*, JHEP **04** (2015) 101, arXiv:1501.06569.

[6] A. V. Manohar, *The decays $Z \to W\pi$ and $Z \to \gamma\pi$*, Phys. Lett. **B244** (1990) 101.

[7] ATLAS collaboration, G. Aad *et al.*, *Search for Higgs and Z boson decays to $J/\psi\gamma$ and $\Upsilon(nS)\gamma$ with the ATLAS detector*, Phys. Rev. Lett. **114** (2015) 121801, arXiv:1501.03276.

[8] ATLAS collaboration, M. Aaboud *et al.*, *Search for Higgs and Z boson decays to $\phi\gamma$ with the ATLAS detector*, Phys. Rev. Lett. **117** (2016) 111802, arXiv:1607.03400.

[9] ATLAS collaboration, M. Aaboud *et al.*, *Search for exclusive Higgs and Z boson decays to $\phi\gamma$ and $\rho\gamma$ with the ATLAS detector*, JHEP **07** (2018) 127, arXiv:1712.02758.

[10] ATLAS collaboration, M. Aaboud *et al.*, *Searches for exclusive Higgs and Z boson decays into $J/\psi\gamma$, $\psi(2S)\gamma$ and $\Upsilon(nS)\gamma$ at $\sqrt{s} = 13$ TeV with the ATLAS detector*, Phys. Lett. **B786** (2018) 134, arXiv:1807.00802.

[11] CMS collaboration, A. M. Sirunyan *et al.*, *Search for rare decays of Z and Higgs bosons to J/ψ and a photon in proton-proton collisions at $\sqrt{s} = 13$ TeV*, Eur. Phys. J. **C79** (2019) 94, arXiv:1810.10056.

[12] CMS collaboration, A. M. Sirunyan *et al.*, *Observation of the $Z \to \psi\ell^+\ell^-$ decay in pp collisions at $\sqrt{s} = 13$ TeV*, Phys. Rev. Lett. **121** (2018) 141801, arXiv:1806.04213.

[13] CDF collaboration, F. Abe *et al.*, *Search for the rare decay $W^\pm \to D_s^\pm\gamma$ in $p\bar{p}$ collisions at $\sqrt{s} = 1.8$ TeV*, Phys. Rev. **D58** (1998) 091101.

[14] A. L. Kagan *et al.*, *Exclusive window onto Higgs Yukawa couplings*, Phys. Rev. Lett. **114** (2015) 101802, `arXiv:1406.1722`.

[15] LHCb collaboration, A. A. Alves Jr. *et al.*, *The LHCb detector at the LHC*, JINST **3** (2008) S08005.

[16] LHCb collaboration, R. Aaij *et al.*, *LHCb detector performance*, Int. J. Mod. Phys. **A30** (2015) 1530022, `arXiv:1412.6352`.

[17] R. Aaij *et al.*, *Performance of the LHCb Vertex Locator*, JINST **9** (2014) P09007, `arXiv:1405.7808`.

[18] R. Arink *et al.*, *Performance of the LHCb Outer Tracker*, JINST **9** (2014) P01002, `arXiv:1311.3893`.

[19] P. d'Argent *et al.*, *Improved performance of the LHCb Outer Tracker in LHC Run 2*, JINST **12** (2017) P11016, `arXiv:1708.00819`.

[20] M. Adinolfi *et al.*, *Performance of the LHCb RICH detector at the LHC*, Eur. Phys. J. **C73** (2013) 2431, `arXiv:1211.6759`.

[21] C. Abellan Beteta *et al.*, *Calibration and performance of the LHCb calorimeters in Run 1 and 2 at the LHC*, `arXiv:2008.11556`, submitted to JINST.

[22] A. A. Alves Jr. *et al.*, *Performance of the LHCb muon system*, JINST **8** (2013) P02022, `arXiv:1211.1346`.

[23] G. Dujany and B. Storaci, *Real-time alignment and calibration of the LHCb Detector in Run II*, J. Phys. Conf. Ser. **664** (2015) 082010.

[24] R. Aaij *et al.*, *The LHCb trigger and its performance in 2011*, JINST **8** (2013) P04022, `arXiv:1211.3055`.

[25] R. Aaij *et al.*, *Tesla: an application for real-time data analysis in High Energy Physics*, Comput. Phys. Commun. **208** (2016) 35, `arXiv:1604.05596`.

[26] T. Sjöstrand, S. Mrenna, and P. Skands, *A brief introduction to PYTHIA 8.1*, Comput. Phys. Commun. **178** (2008) 852, `arXiv:0710.3820`.

[27] I. Belyaev *et al.*, *Handling of the generation of primary events in Gauss, the LHCb simulation framework*, J. Phys. Conf. Ser. **331** (2011) 032047.

[28] D. J. Lange, *The EvtGen particle decay simulation package*, Nucl. Instrum. Meth. **A462** (2001) 152.

[29] N. Davidson, T. Przedzinski, and Z. Was, *PHOTOS interface in C++: Technical and physics documentation*, Comp. Phys. Comm. **199** (2016) 86, `arXiv:1011.0937`.

[30] Geant4 collaboration, J. Allison *et al.*, *Geant4 developments and applications*, IEEE Trans. Nucl. Sci. **53** (2006) 270; Geant4 collaboration, S. Agostinelli *et al.*, *Geant4: A simulation toolkit*, Nucl. Instrum. Meth. **A506** (2003) 250.

[31] M. Clemencic *et al.*, *The LHCb simulation application, Gauss: Design, evolution and experience*, J. Phys. Conf. Ser. **331** (2011) 032023.

[32] V. V. Gligorov and M. Williams, *Efficient, reliable and fast high-level triggering using a bonsai boosted decision tree*, JINST **8** (2013) P02013, `arXiv:1210.6861`.

[33] M. Calvo Gomez *et al.*, *A tool for γ/π^0 separation at high energies*, LHCb-PUB-2015-016, CERN-LHCb-PUB-2015-016, 2015.

[34] LHCb collaboration, R. Aaij *et al.*, *Measurement of forward W and Z boson production in pp collisions at $\sqrt{s} = 8$ TeV*, JHEP **01** (2016) 155, `arXiv:1511.08039`.

[35] LHCb collaboration, R. Aaij *et al.*, *Precision measurement of forward Z boson production in proton-proton collisions at $\sqrt{s} = 13$ TeV*, JHEP **07** (2022) 026, `arXiv:2112.07458`.

[36] W. Barter, M. Pili, and M. Vesterinen, *A simple method to determine charge-dependent curvature biases in track reconstruction in hadron collider experiments*, Eur. Phys. J. **C81** (2021) .

[37] R. J. Barlow and C. Beeston, *Fitting using finite Monte Carlo samples*, Comput. Phys. Commun. **77** (1993) 219.

[38] A. L. Read, *Presentation of search results: the CL_s technique*, J. Phys. G:Nucl. Part. Phys. **28** (2002) 2693.

[39] T. Junk, *Confidence level computation for combining searches with small statistics*, Nuclear Instruments and Methods in Physics Research Section A: Accelerators, Spectrometers, Detectors and Associated Equipment **434** (1999) 435.

[40] L. Moneta *et al.*, *The RooStats project*, PoS **ACAT2010** (2010) 057, `arXiv:1009.1003`.

[41] G. Cowan, K. Cranmer, E. Gross, and O. Vitells, *Asymptotic formulae for likelihood-based tests of new physics*, Eur. Phys. J. **C71** (2011) 1554, `arXiv:1007.1727`.

[42] ATLAS collaboration, G. Aad *et al.*, *Measurement of the cross-section of high transverse momentum $Z \to b\bar{b}$ production in proton–proton collisions at $\sqrt{s} = 8 TeV$ with the ATLAS detector*, Phys. Lett. **B738** (2014) 25, `arXiv:1404.7042`.

[43] ATLAS collaboration, G. Aad *et al.*, *Identification of boosted, hadronically decaying W bosons and comparisons with ATLAS data taken at $\sqrt{s} = 8$ TeV*, Eur. Phys. J. **C76** (2016) 154, `arXiv:1510.05821`.

[44] K. S. Cranmer, *Kernel estimation in high-energy physics*, Comput. Phys. Commun. **136** (2001) 198, `arXiv:hep-ex/0011057`.

[45] LHCb collaboration, R. Aaij *et al.*, *Measurement of the track reconstruction efficiency at LHCb*, JINST **10** (2015) P02007, `arXiv:1408.1251`.

[46] L. Anderlini *et al.*, *The PIDCalib package*, LHCb-PUB-2016-021, 2016.

[47] R. Aaij *et al.*, *Selection and processing of calibration samples to measure the particle identification performance of the LHCb experiment in Run 2*, Eur. Phys. J. Tech. Instr. **6** (2019) 1, arXiv:1803.00824.

[48] LHCb collaboration, R. Aaij *et al.*, *Measurement of the $D_s^+ - D_s^-$ production asymmetry in 7 TeV pp collisions*, Phys. Lett. **B713** (2012) 186, arXiv:1205.0897.

[49] Particle Data Group, R. L. Workman, *Review of Particle Physics*, PTEP **2022** (2022) 083C01.

[50] LHCb collaboration, *Expression of Interest for a Phase-II LHCb Upgrade: Opportunities in flavour physics, and beyond, in the HL-LHC era*, CERN-LHCC-2017-003, 2017.